Unmanned Systems, Vol. 14, No. 1 (2026) 7–19

DOI: 10.1142/S2301385025500773

UNMANNED SYSTEMS
https://www.worldscientific.com/worldscinet/us

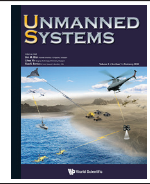


# Radio Environment Map Construction by Residual Kriging Based on Bayesian Hierarchical Model

Haiyang Xia [*], Song Zha [†,‖], Hao Ding [‡,‖], Jijun Huan [§], Peiguo Liu [¶]

*College of Electronic Science and Engineering,*
*National University of Defense Technology, No. 109, Deya Road, Changsha 410073, P. R. China*

Radio environment maps (REMs) have demonstrated their significance in spectrum sensing, control, and sharing, particularly in relation to unmanned systems, the Internet of Things (IoT), and 5G communication. However, they encounter challenges related to meeting the increasing accuracy requirements. This paper introduces the BHM-RK algorithm, a novel approach for constructing REMs in scenarios with multiple transmitters. The algorithm utilizes spatial clustering for transmitter partitioning, Bayesian posterior inference within partitions, and residual Kriging interpolation to address challenges posed by diverse transmitter influences. Experimental validation demonstrates the superior performance of the BHM-RK algorithm in terms of construction accuracy compared to existing methods, highlighting its effectiveness in enhancing precision in REM construction for scenarios with multiple transmitters.

*Keywords*: Radio environment maps (REMs); spatial clustering; Bayesian; residual Kriging; pathloss; shadow fading.

## 1. Introduction

In the realm of spatial spectrum sharing, radio environment maps (REMs) [1] have garnered significant attention due to their pivotal role in facilitating uninterrupted communication services for unmanned systems, the Internet of Things (IoT), 5G communication and high-power shielding [2, 3]. REMs serve as crucial tools for perceiving and managing the electromagnetic environment, providing essential support for users. The development of REM construction methods has been a focal point in this area. However, challenges persist: indirect techniques often necessitate an abundance of prior information, while direct methods may overlook pertinent data, thus impacting the accuracy of REMs [4] within the wireless communication industry.

While spatial statistics methods fall under the category of direct methods, their potential has been increasingly recognized in recent years. Riihijarvi [5] characterized and modeled spectrum maps using random field and semi-variogram techniques. Additionally, Sato [6] applied ordinary Kriging (OK) interpolation to estimate interference power for primary users, while Xia [7] enhanced the Kriging approach by incorporating affinity propagation clustering for rapid REM construction. Spatial statistics methods excel in depicting random fields by leveraging spatial correlation structures, with the shadow fading component of empirical propagation models serving as a quintessential example of a spatial random field [8].

In addition to the random component, the deterministic aspect of a propagation model illustrates signal attenuation between transmitter and receiver using model parameters. However, these parameters exhibit variability due to spatial and temporal changes, necessitating their acquisition in a specific area prior to each REM construction. Bayesian hierarchical models (BHMs) [9] are widely acknowledged as cutting-edge techniques for estimating model parameters. Typically, radio propagation is considered as a prior, and measurements are employed as likelihood to construct the Bayesian model. The posterior inference of parameters can be theoretically computed through integration or summation.

Received 8 April 2024; Accepted 22 September 2024; Published 21 November 2024. This paper was recommended for publication in its revised form by editorial board member, Kai Yang.
Email Addresses: *[*]easonhsia@sina.com*, *[†]zhasong0551@163.com*, *[‡]dinghao20a@nudt.edu.cn*, *[§]huangjijun1989@nudt.edu.cn*, *[¶]pg731@126.com*
[‖]Corresponding authors.

Nevertheless, Markov chain Monte Carlo (MCMC) algorithms are considered more suitable for engineering solutions due to their approximation capabilities, particularly in scenarios where obtaining exact posterior quantities is challenging or infeasible [10]. The approach described in [11] leverages MCMC within BHM estimation, albeit requiring pre-training prior to inference and direct implementation using the "Stan" software, which may pose challenges for integration into comprehensive systems. Among the Metropolis–Hastings algorithms [12], Gibbs sampling [13] stands out as superior in this context, given its high acceptance rate of proposals and the ability to derive conditional probability distributions through mathematical deduction.

BHM excels in single-transmitter scenarios [14]. Yet, it struggles with propagation in multi-transmitter settings, reducing its urban practicality where such setups are common. Therefore, partitioning transmitters before BHM application is crucial. Leveraging the low overlap in coverage areas of co-frequency transmitters, spatial clustering by received power effectively delineates these areas. This method refines measurement differentiation by segmenting multi-transmitter zones into single-transmitter sub-areas, optimizing data for BHM.

Prior to partitioning, trend surface fitting and spatial clustering are crucial processes. The generalized regression neural network (GRNN) algorithm [15] is known for providing smooth transitions between observed values and nonlinear modeling during trend surface fitting. For spatial clustering, drawing inspiration from density-based spatial clustering of applications with noise (DBSCAN) [16], the coverage range of transmitters serves as a reliable reference for determining the clustering neighborhood radius parameter. By leveraging the electromagnetic characteristics near the transmitter, density determination can be replaced with a dual verification of intensity and gradient, effectively resolving the transmitter partitioning challenge.

This study introduces the BHM-RK algorithm, which presents an innovative approach for developing REMs tailored to multi-transmitter scenarios. The methodology includes spatial clustering for transmitter partitioning to differentiate measurements, Bayesian posterior inference of empirical propagation parameters within partitions, and residual Kriging for estimating the shadow fading component. In contrast to our previously published proceedings [14], this paper delineates two significant advancements, i.e. applicability expansion to multi-transmitter scenarios and integration of real-world data testing with synthetic counterparts. Hence, the main contributions of this paper include the following:

(1) The proposed algorithm successfully tackles the complex challenges posed by scenarios involving diverse transmitters through innovative spatial clustering for transmitter partitioning.
(2) Furthermore, it integrates Gibbs sampling into BHM analysis in a creative manner, enhancing the accuracy of REM construction.
(3) To substantiate the algorithm's superior accuracy, this paper employs a robust validation approach, encompassing not just synthetic data tests but also real-world scenarios for comprehensive evaluation.

The remaining part of this paper is organized as follows: Sec. 2 outlines the system model and problem statement while Sec. 3 provides the BHM-RK algorithm in detail. Experimental results and performance analysis are presented in Sec. 4. Eventually, Sec. 5 concludes this paper.

## 2. System Model and Problem Statement

In this paper, the area of interest is considered as a two-dimensional space denoted by $\boldsymbol{l} \in \mathbb{R}^2$, within which a set of sensors are placed on $\{l_r\}_{r=1}^R$, and the received signal strength (RSS) is denoted by $\{z_r\}_{r=1}^R$, which can be expressed in the form of vectors as $\mathbf{L} = [l_1, l_2, \ldots, l_R]^\top$ and $\mathbf{Z} = [z_1, z_2, \ldots, z_R]^\top$ respectively. According to the signal propagation model, the RSS of $r$th sensor can be denoted as

$$z_r = \nu_r + s_r + \iota_r + n_r, \quad r = 1, 2, \ldots, R,$$

where $\nu_r$ is the pathloss component, $s_r$ is the shadow fading component, $\iota_r$ is the fast fading and $n_r$ is the measurement error caused by devices. Whereas path loss and shadowing typically vary in a scale of meters, fast fading changes in a scale comparable to the wave-length [17]. Since this paper focuses on the band of UHF, which means the fast fading changes in a scale between centimeter and decimeter, which requires the knowledge of sensor locations with an accuracy in the order of centimeter, which is inaccessible due to the current localization system of sensors. Thus, it is customary to assume that the effects of fast fading have been averaged out. Meanwhile, $n_r$ can be eliminated by multiple measurements. Hence, the RSS is only decomposed into pathloss and shadow fading components in this paper.

The pathloss component $\nu_r$ of $r$th sensor describes the signal attenuation as

$$\nu_r = 10 \log_{10}\left(\sum_{t=1}^{T} 10^{\frac{\nu_{r,t}}{10}}\right), \quad r = 1, 2, \ldots, R \tag{1}$$

and the pathloss component $\nu_{r,t}$ of $r$th sensor receiving from the $t$th transmitter can be described as

$$\nu_{r,t} = P_t - G_{dB} - 10\eta \log_{10}\left(\frac{\|l_t - l_r\|}{d_0}\right), \quad r = 1, 2, \ldots, R, \tag{2}$$

where $P_t$ is the transmitting power, $l_t$ is the transmitter's location, $\eta$ is the pathloss exponent, $\|l_t - l_r\|$ is the Euclidean distance between $l_t$ and $l_r$, $d_0$ is the reference distance for antenna far field, $G_{\text{dB}} = 20\log_{10}(4\pi d_0/\lambda)$ is the pathloss factor, which is a function of signal propagation wavelength $\lambda$.

The shadow fading component describes a random phenomenon modeled by a log-normal distribution with zero mean. Sensors received more correlated shadow fading components when their locations are closer, and the Gudmundson model [18] can be employed for the spatial correlation

$$\Psi(i,j) = \sigma_c^2 \exp\left(-\frac{\|l_i - l_j\|}{d_c}\right), \tag{3}$$

where $\sigma_c$ is the standard deviation and $d_c$ is the correlation distance of shadow fading.

However, since the sensors are usually placed dispersedly [19] within the region, the relation between sensors' distances and correlation distance can be expressed as

$$\|l_i - l_j\| \gg d_c, \quad l_{i,j} \in \mathbf{L}. \tag{4}$$

Consequently, the measurements can be expressed by a Gaussian distribution with mean vector and covariance matrix

$$\mathrm{E}[\tilde{\mathbf{Z}}] = P_t - G_{dB} - 10\eta\log_{10}\left(\frac{\|l_t - \mathbf{L}\|}{d_0}\right), \tag{5}$$

$$\mathrm{Var}[\tilde{\mathbf{Z}}] \approx \sigma_c^2 \mathbf{I}_R, \tag{6}$$

where $\mathbf{I}_R$ is the $R \times R$ identity matrix.

The objective of this paper, conducted in a multi-transmitter scenario, is to obtain the accurate REM $\{\hat{z}_k | l_k \in \mathbf{l}\}$ according to the $\{z_r\}_{r=1}^R$, $\{l_r\}_{r=1}^R$ and prior distributions of propagation model parameters $\boldsymbol{\xi} = [P_t, \eta, \sigma_c^2]$, through spatial clustering for transmitters partition, Bayesian estimation via Gibbs sampling for pathloss component and residual Kriging interpolation for shadow fading component.

## 3. Residual Kriging Based on Bayesian Hierarchical Model

To address this problem, the proposed algorithm can be separated into three steps: (1) spatial clustering for transmitters partition, (2) Bayesian posterior inference in each partition and (3) residual Kriging interpolation. First, the process of transmitters partition includes GRNN for trend surface fitting as well as spatial clustering based on dual verification. Then Bayesian posterior inference is composed of BHM construction of parameters and Gibbs sampling for posterior estimation. Last, residual Kriging is applied for estimation of shadow fading. The pictorial representation of BHM-RK is shown in Fig. 1. Procedures are described as follows in detail.

### 3.1. *Spatial clustering for multiple transmitters partition*

#### 3.1.1. *Generalized regression neural network for trend surface fitting*

The GRNN algorithm is a variant of the RBF neural network algorithm with a highly parallel structure and a one-pass learning approach. A GRNN consists of four layers, namely, an input layer, a pattern layer, a summation layer, and an output layer, as shown in Fig. 2. The input layer contains

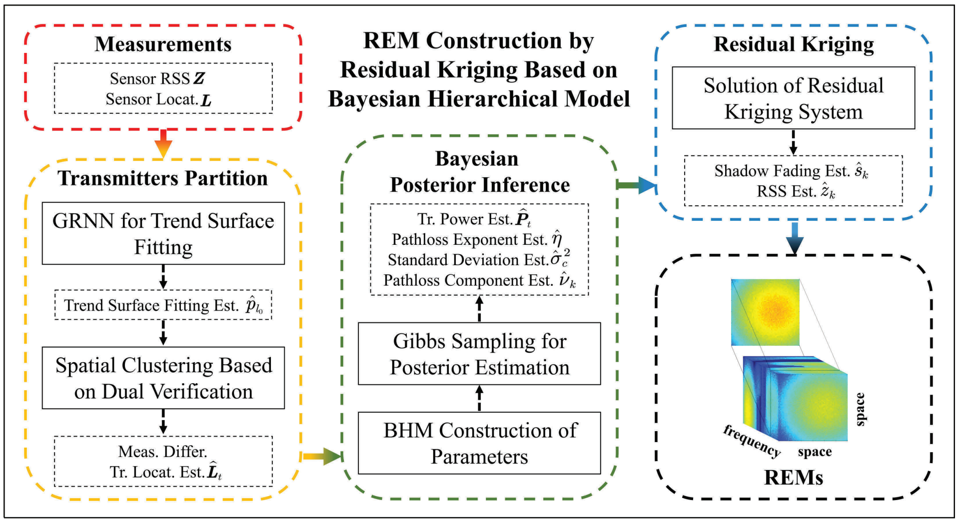


Fig. 1. Pictorial representation of REM construction by residual Kriging based on BHM.

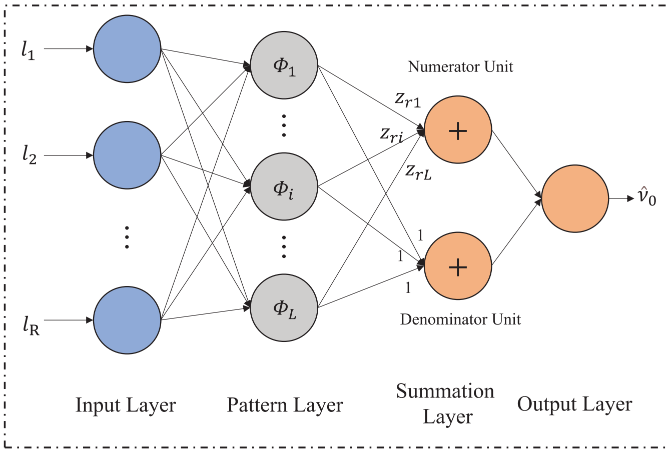


Fig. 2. Structure of a GRNN.

neurons whose transfer functions are linear, and they are equal in number to the dimensions of the input vector. The pattern layer is the radial basis layer, and each neuron in this layer uses a radial basis function as its activation function, for which a Gaussian function is commonly adopted:

$$\Phi_i(l_0) = \exp\left(-\frac{\|l_0 - c_i\|^2}{2\sigma_g^2}\right), \tag{7}$$

where $c_i$ is the center vector, and $\sigma_g$ is a smoothing parameter controlling the spread of the radial basis function.

The summation layer contains two types of neurons: a numerator unit and a denominator unit. The numerator unit is used to calculate a weighted sum of the neurons in the pattern layer, while the denominator unit is used to calculate the algebraic sum. Finally, the results of trend surface fitting are expressed as

$$\hat{p_{l_0}} = \frac{\sum_{i=1}^{L} \Phi_i(l_0) z_{ri}}{\sum_{i=1}^{L} \Phi_i(l_0)}, \quad r = 1, 2, \ldots, R. \tag{8}$$

### 3.1.2. *Spatial clustering based on dual verification of intensity and gradient*

Given that the effective coverage areas of transmitters operating in the same frequency band exhibit relatively low overlap under normal working conditions, their distances from each other are considerable. Therefore, the critical part in this step lies in selecting the area to suspected transmitter regions. This area is subjected to spatial clustering to effectively partition the multiple transmitters. Subsequently, spatial differentiation of measurements can be conducted to prepare the data more precisely for the afterward BHM.

Considering the characteristics of GRNN for trend surface fitting, the areas near transmitters are bound to exhibit two features: (1) relatively high received power, i.e. large intensity values; (2) relatively smooth changes, i.e. small gradient values (it is worth noting that in reality, the variation in received power near transmitters is rather intense, which differs from the results of trend surface fitting). Therefore, in the context of trend surface fitting results, regions that simultaneously satisfy the above two features can be identified by setting a proportional threshold, thus forming a collection of suspected transmitter-adjacent areas.

The set satisfying the first intense features, $\Delta_{\text{inten}}$, can be represented as

$$\Delta_{\text{inten}} := \left\{ \begin{array}{c} l \in \boldsymbol{l} | \hat{p}_l \geq \hat{p}_{l'}, l' \in \boldsymbol{l}', \boldsymbol{l}' \subseteq \boldsymbol{l}, \\ \dfrac{\|\boldsymbol{l}'\|_0}{\|\boldsymbol{l}\|_0} \geq (1 - \rho_{\text{inten}}) \end{array} \right\}, \tag{9}$$

where $\hat{p}_l$ is the RSS intense at the location $l$, $\|\cdot\|_0$ is the $l_0$-norm, $\rho_{\text{inten}}$ is the intense proportional threshold.

Meanwhile, the set satisfying the second gradient features, $\Delta_{\text{grad}}$, can be represented as

$$\Delta_{\text{grad}} := \left\{ \begin{array}{c} l \in \boldsymbol{l} | \hat{q}_l \leq \hat{q}_{l''}, l'' \in \boldsymbol{l}'', \boldsymbol{l}'' \subseteq \boldsymbol{l}, \\ \dfrac{\|\boldsymbol{l}''\|_0}{\|\boldsymbol{l}\|_0} \geq (1 - \rho_{\text{grad}}) \end{array} \right\}, \tag{10}$$

where $\hat{q}_l$ is the gradient at the location $l$, $\rho_{\text{grad}}$ is the gradient proportional threshold.

Therefore, the set of suspected transmitter-adjacent areas $\Delta_{\text{STAs}}$ can be obtained by

$$\Delta_{\text{STAs}} = \Delta_{\text{inten}} \cap \Delta_{\text{grad}}. \tag{11}$$

To further perform spatial differentiation on the measurements, spatial clustering is used to cluster suspected transmitter-adjacent areas. It is based on the density of suspected transmitter-adjacent areas and is effective in identifying regions of high density while categorizing sparse areas as noise points, which can effectively reduce the interference caused by outliers. For $\Delta_{\text{STAs}}$, the clusters $\Delta_{\text{Eps}}$ are created depending on the spatial distance threshold $d_{\text{Eps}}$

$$\Delta_{\text{Eps}} := \{ l \in \Delta_{\text{STAs}} | \|l' - l\|_2 < d_{\text{Eps}}, l' \in \Delta_{\text{STAs}} \}, \tag{12}$$

where $\|\cdot\|_2$ is the $l_2$-norm.

The centroids $l^{\ddagger}$, where the sum of its Euclidean distances to all other points within the cluster is minimized, can be obtained by

$$\min_{l^{\ddagger} \in \Delta_{\text{Eps}}} \sum_{l''} \|l^{\ddagger} - l''\|_2, \quad l'' \in \Delta_{\text{Eps}}. \tag{13}$$

Then, the spatial differentiation of measurements can be determined by calculating the distance between measurements and the centroids of each cluster.

### 3.2. *Gibbs sampling of Bayesian posterior inference for pathloss*

The Bayesian prior represents the initial belief or knowledge about an unknown parameter in Bayesian estimation. It encapsulates subjective or objective information before any data is observed. The prior distribution serves as the starting point for updating our knowledge using Bayes' theorem. By incorporating prior knowledge, we can shape the posterior distribution, which combines the prior and likelihood from the observed data. The influence of the prior on the posterior depends on its weight and compatibility with the data.

After the spatial differentiation of measurements, the solving of BHM in a multi-transmitter scenario can be approximately transformed into solving it in a single-transmitter scenario. Because, the received signal in suspected transmitter-adjacent areas is significantly more influenced by nearby transmitters than by others.

Then, the Bayesian approach to parameter estimation in this work can be to treat $\boldsymbol{\xi} = [P_t, \eta, \sigma_c^2]$ as random variables, which are associated with prior distributions. The prior distributions show how likely the parameter values are before any measurements are observed by sensors. Using Bayes rule, the conditional probability can be written as $f(\boldsymbol{\xi}|\tilde{\mathbf{Z}}_m) \propto f(\boldsymbol{\xi})f(\tilde{\mathbf{Z}}_m|\boldsymbol{\xi})$. Therefore, within the spatial differentiation of measurement discussed above, the BHM has been constructed by these parameters, see in Fig. 3

For model parameters $\boldsymbol{\xi}$, we choose following prior distributions based on their empirical ranges and the "weak informative" theory [11], which can be expressed as $P_t \sim \text{Normal}(\mu_{P_t}, \sigma_{P_t}^2), \eta \sim \text{Normal}(\mu_\eta, \sigma_\eta^2)$ and $\sigma_c^2 \sim$ Inverse Gamma$(\alpha, \beta)$. Then, the separate inferential statement of parameters can be made according to the integration of likelihood and prior.

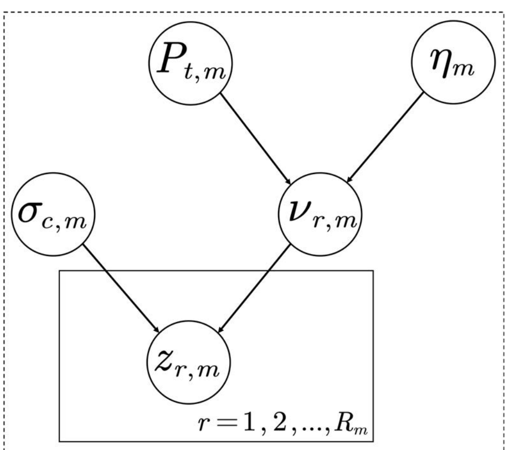


Fig. 3. Graphic BHM within each spatial differentiation of measurements.

However, it is impossible to find out closed-form for this integration in practice. So, we have to resort to approximate inference methods based on numerical sampling, also known as MCMC, which can process the estimation based on the posterior distributions instead of exact integral calculations.

The conditional distributions of model parameters, whose rigorous deductions are formulated in Appendix A, are given as follows:

$$P_{t,m}{}^{\text{post}} \sim \text{Normal}(\mu_{P_t}{}^\dagger, \sigma_{P_t}^2{}^\dagger), \tag{14}$$

$$\eta^{\text{post}} \sim \text{Normal}(\mu_\eta{}^\dagger, \sigma_\eta^{2\dagger}), \tag{15}$$

$$\sigma_c^{2\text{post}} \sim \text{InverseGamma}(\alpha^\dagger, \beta^\dagger), \tag{16}$$

where

$$\sigma_{P_{t,m}}^2{}^\dagger = \left( \frac{1}{\sigma_{P_{t,m}}^2} + \frac{R}{\sigma_c^2} \right)^{-1}, \tag{17}$$

$$\mu_{P_{t,m}}{}^\dagger = \sigma_{P_{t,m}}^2{}^\dagger \left\{ \frac{\mu_{P_{t,m}}}{\sigma_{P_{t,m}}^2} + \frac{1}{\sigma_c^2} \sum_{r=1}^{R} \left[ \begin{matrix} z_r + G_{dB} + \\ 10\eta \cdot DL(r) \end{matrix} \right] \right\}, \tag{18}$$

$$\sigma_\eta^{2\dagger} = \left[ \frac{1}{\sigma_\eta^2} + \frac{10}{\sigma_c^2} \sum_{r=1}^{R} DL(r) \right]^{-1}, \tag{19}$$

$$\mu_\eta{}^\dagger = \sigma_\eta^{2\dagger} \left\{ \frac{\mu_\eta}{\sigma_\eta^2} - \frac{10}{\sigma_c^2} \sum_{r=1}^{R} \left[ \begin{matrix} DL(r) \cdot \\ (z_r - P_t + G_{dB}) \end{matrix} \right] \right\}, \tag{20}$$

$$\alpha^\dagger = \alpha + \frac{R}{2}, \tag{21}$$

$$\beta^\dagger = \left\{ \frac{1}{\beta} + \frac{1}{2} \sum_{r=1}^{R} \left[ \begin{matrix} z_r - P_t + G_{dB} + \\ 10\eta \cdot DL(r) \end{matrix} \right] \right\}^{-1}, \tag{22}$$

where $DL(r) \doteq \log_{10}(\|l_t - l_r\|/d_0)$.

This leads to the following Gibbs sampling procedure where the state at iteration $n$ consists of sampled values $P_{t,m}{}^{\text{post}}(n)$, $\eta^{\text{post}}(n)$ and $\sigma_c^{2\text{post}}(n)$:

(1) Set iteration $n = 1$ and maximum iteration limitation $N$.
(2) Generate initial values $P_{t,m}{}^{\text{post}}(1)$, $\eta^{\text{post}}(1)$ and $\sigma_c^{2\text{post}}(1)$.
(3) Repeat
$n = n + 1$
Sample
$P_{t,m}{}^{\text{post}}(n) \sim f(P_{t,m}{}^{\text{post}}|\tilde{\mathbf{Z}}, \eta^{\text{post}}(n-1), \sigma_c^{2\text{post}}(n-1))$ from (14), (17) and (18)
Sample
$\eta^{\text{post}}(n) \sim f(\eta^{\text{post}}|\tilde{\mathbf{Z}}, P_t{}^{\text{post}}(n), \sigma_c^{2\text{post}}(n-1))$ from (15), (19) and (20)

Sample $\sigma_c^{2\text{post}}(n) \sim f(\sigma_c^{2\text{post}}|\tilde{\mathbf{Z}}, P_t{}^{\text{post}}(n), \eta^{\text{post}}(n))$ from (16), (21) and (22)

(4) Until $n = N$.

Therefore, for each spatial differentiation of measurements, the transmitting power and locations of each transmitter can be described as

$$\hat{\boldsymbol{P}}_t = \{\hat{P}_{t,m}, m = 1, 2, \ldots, M\}, \tag{23}$$

$$\hat{\boldsymbol{L}}_t = \{l_m^{\ddagger}, m = 1, 2, \ldots, M\}, \tag{24}$$

where $M$ is the number of differentiation. Also,

$$\hat{\eta} = \sum_{m=1}^{M} \hat{\eta}_m, \tag{25}$$

$$\hat{\sigma}_c^2 = \sum_{m=1}^{M} \hat{\sigma}_{c,m}^2. \tag{26}$$

Hence, the pathloss component estimation $\hat{\nu}_k, l_k \in \boldsymbol{l}$ can be obtained from (1), (2), (23)–(25).

### 3.3. *Residual Kriging for Shadow fading*

After the pathloss inference, the measurement residuals $\tilde{s}_r$, which are employed for Kriging interpolation to estimate the shadow fading, can be obtained by

$$\tilde{s}_r = \tilde{z}_r - \hat{\nu}_r, \quad r = 1, 2, \ldots, R. \tag{27}$$

OK is geostatistical best linear unbiased estimator for second-order stationary or intrinsic spatial random field [20], the log-normal distributive shadow fading component fulfills this prerequisite.

Before the interpolation, semi-variogram needs to be modeled to estimate the spatial covariance structure of measurement residuals. In consideration of spatial correlation of shadow fading in (2), the exponent model is chosen for semi-variogram, which is represented as

$$\gamma(l_i, l_j) = C_0 + C\left[1 - \exp\left(-\frac{\|l_i - l_j\|}{a}\right)\right], \quad l_{i,j} \in \boldsymbol{l}, \tag{28}$$

where $C_0$ is the nuggets, $C_0 + C$ is the sill and $a$ is the range.

Next, the shadow fading component $\hat{s}_k$ within the region of interest can be expressed as

$$\hat{s}_k = \sum_{r=1}^{R} \omega_{r|k} \cdot \tilde{s}_r, \quad l_k \in \boldsymbol{l}, \tag{29}$$

where $\omega_{r|k}$ is the weight assigned for $r$th sensor of $l_k$, which fulfills the unbiased condition, namely, $\sum_{r=1}^{R} \omega_{r|k} = 1, l_k \in \boldsymbol{l}$.

They can be obtained by solving the Kriging system, which is expressed as

$$\sum_{r=1}^{R} \omega_{r|k} \cdot \gamma(l_r, l_{r'}) + \mathcal{L}_k = \gamma(l_r, l_k), \quad r' = 1, 2, \ldots, R, \quad l_k \in \boldsymbol{l}, \tag{30}$$

where $\mathcal{L}_k$ is the Lagrange multiplier.

Hence, the accurate REM can be obtained by these two estimated components

$$\hat{z}_k = \hat{\nu}_k + \hat{s}_k, \quad l_k \in \boldsymbol{l}. \tag{31}$$

## 4. Experimental Results and Performance Analysis

### 4.1. *Control groups and evaluation metrics*

In this section, the proposed algorithm is validated through synthetic data test as well as real-world data test. To evaluate the performance of the proposed method, we choose the BHM without shadow fading estimation, OK [20], GRNN [15], natural neighbor interpolation (NNI) [5] and inverse distance weighted (IDW) [21] as control groups.

Meanwhile, we apply the root mean squared error (RMSE) to represent REM construction accuracy of different algorithms as well as the mean absolute error (MAE) to compare the transmitting power estimations at transmitters' locations. Specifically, to validate the proposed method's accuracy in estimating the pathloss exponent and standard deviation, we also introduce the parameter error ratio (PER). They are defined as follows:

$$e_{\text{RMSE}} = \sqrt{\frac{1}{\|\boldsymbol{l}\|_0} \sum_{\|\boldsymbol{l}\|_0} (\hat{z}_k - z_k)^2}, \quad l_k \in \boldsymbol{l}, \tag{32}$$

where $\|\boldsymbol{l}\|_0$ is the $l_0$-norm of $\boldsymbol{l}$, representing the size of area of interest, and

$$e_{\text{MAE}} = \frac{1}{T} \sum_{t=1}^{T} |\hat{P}_{t,m} - P_t|, \tag{33}$$

where $T$ is the number of transmitters, and

$$e_{\text{PER}} = \frac{|\hat{\xi} - \xi|}{\xi} \times 100\%, \tag{34}$$

where $\xi = [\eta, \sigma_c^2]$.

### 4.2. *Synthetic data test case*

The synthetic data test is conducted based on the scenarios introduced in Sec. 2 and the parameter settings in Table 1, which are used to simulate the power transmission in the

Table 1. Simulation environment parameters setting.

| Parameters | Value |
|---|---|
| Transmitting power | 30 dBm and 27 dBm |
| Frequency | 2630 MHz |
| Pathloss exponent | 3.0 |
| Reference distance | 5 m |
| Correlation distance | 1 m |
| Prior mean of transmitting power | 36 dBm |
| Prior variance of transmitting power | 4 |
| Prior mean of pathloss exponent | 4.0 |
| Prior variance of pathloss exponent | 4 |
| Prior shape of standard deviation square | 2.0 |
| Prior scale of standard deviation square | 0.0625 |

downlink frequency band of 5G base stations. Therefore, both RMSE and MAE can be used to evaluate the performance of the proposed algorithm.

Figures 4 and 5 compare RMSEs versus number of sensors and standard deviation, in which BHM-RK always has the least RMSE, clearly demonstrating that the BHM-RK exhibits the highest precision among these evaluated algorithms.

From Fig. 4, the RMSE values across methods diverge significantly, with BHM-RK emerging as the most accurate, boasting the lowest RMSE. For instance, when the number of sensors reaches 50, BHM-RK achieves an RMSE of 2.15, a notable 29.7% improvement over BHM. Additionally, compared to OK, BHM-RK reduces RMSE by 14.4%, maintaining its supremacy in prediction accuracy. Furthermore, BHM-RK outperforms GRNN, NNI, and IDW by 35.7%, 33.1%, and 20.6% in RMSE, respectively, emphasizing its overall superiority.

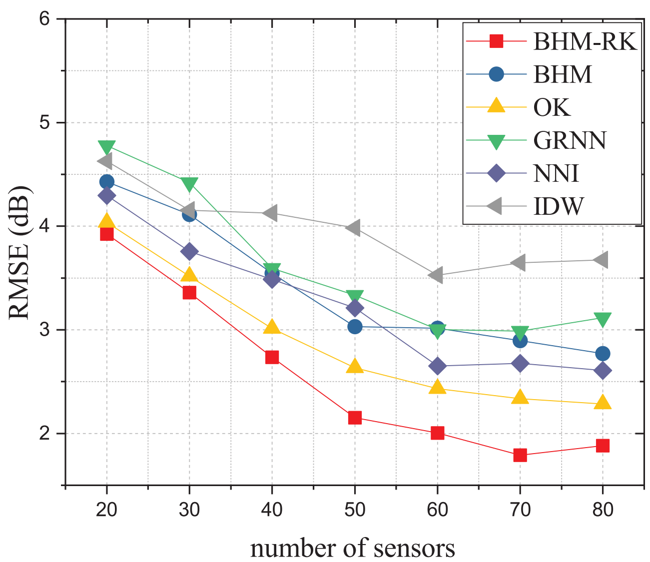


Fig. 4. RMSE versus sensor number with different algorithms, $\sigma_c^2 = 8$.

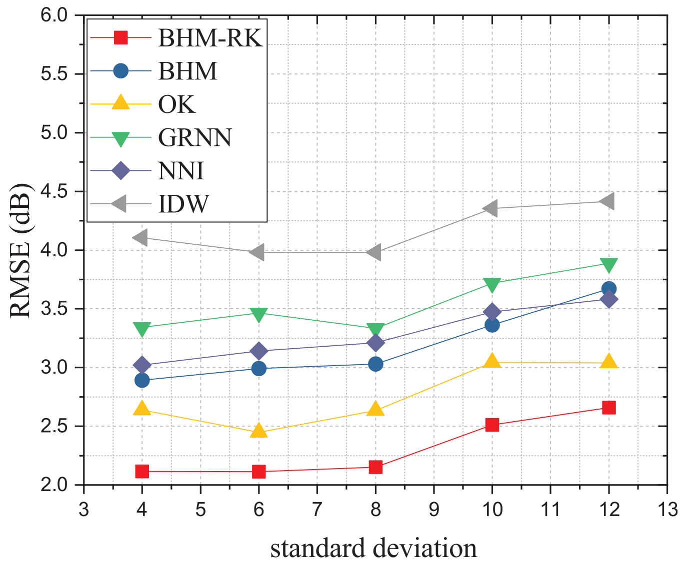


Fig. 5. RMSE versus standard deviation with different algorithms, $R = 50$.

Moreover, in Fig. 4, the trends in RMSE values across methods as sensor numbers rise are noteworthy. Typically, as sensors increase, RMSE values decrease for most methods, signifying accuracy improvements. However, the improvement rates vary. Notably, BHM-RK starts with a low RMSE and continues to decline steadily with more sensors. This implies that BHM-RK is initially accurate and benefits significantly from additional sensors. Conversely, methods like GRNN and IDW exhibit a gradual RMSE decline or even a slight increase with higher sensor counts.

As for Fig. 5, it is evident that as standard deviation increases, the RMSE values for most methods tend to increase, indicating a decrease in prediction accuracy. Meanwhile, across varying standard deviation values, BHM-RK consistently outperforms other methods in terms of RMSE. At a standard deviation of 4, BHM-RK's RMSE is 2.12, a reduction of 26.6% compared to BHM and 19.7% compared to OK. As the standard deviation increases to 6, BHM-RK maintains its low RMSE of 2.11, outperforming BHM by 29.4% and OK by 13.9%. Similarly, at a standard deviation of 8, BHM-RK improves RMSE by 29.0% over BHM and 18.2% over OK. As the standard deviation further increases, BHM-RK maintains its performance advantage, with RMSE values significantly lower than other methods. For instance, at standard deviations of 10 and 12, BHM-RK's RMSE is, respectively, 25.3% and 27.5% lower than BHM, demonstrating its consistent superiority.

Figures 6 and 7 compare MAEs versus number of sensors and standard deviation. Both BHM-RK and BHM stand out with significantly lower values than the remaining algorithms.

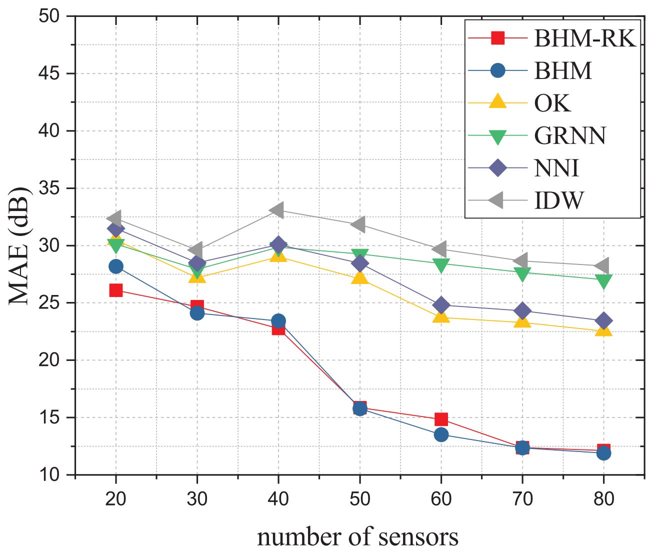


Fig. 6. MAE versus sensor number with different algorithms, $\sigma_c^2 = 8$.

From Fig. 6, when the number of sensors is 50, BHM-RK (or BHM) achieves an MAE value of 15.86, which represents a substantial improvement over the other methods. Compared to OK, BHM-RK (or BHM) outperforms it by approximately 41.5% (27.10 versus 15.86). Similarly, when compared to GRNN, NNI, and IDW, BHM-RK (or BHM) demonstrates a reduction in MAE by 45.9%, 43.2%, and 50.0%, respectively. In Fig. 7, the situation is similar. BHM-RK (or BHM) achieves an MAE of 15.86, reducing the error by approximately 41.5% compared to OK, 45.7% compared to GRNN, 44.0% compared to NNI, and 50.0% compared to IDW.

Notably, while these two methods consistently outperform the others in Figs. 6 and 7, their relative performance varies across different conditions. Specifically, when the number of sensors is low, BHM-RK has a lower MAE than BHM, while BHM achieves a lower MAE when the standard deviation is small. This phenomenon suggests a close competition between them, indicating that both methods are capable of handling the problem of transmitting power estimation.

Figure 8 presents the error ratio values for the BHM method with respect to two parameters, $\eta$ and $\sigma_c^2$, across different standard deviation values. As the standard deviation increases, both $\eta$ and $\sigma_c^2$ display an upward trend in their error ratio values. However, the rate of increase is not uniform for both parameters.

For $\eta$, the error ratio rises more rapidly as the standard deviation increases. Specifically, from a standard deviation of 4 to 6, the error ratio increases by approximately 40% (from 4.38 to 6.13). However, the jump from a standard deviation of 8 to 10 is even more significant, with an increase of over 30% (from 12.31 to 16.06). This trend suggests that the sensitivity of $\eta$ to changes in standard deviation increases as the latter increases.

On the other hand, $\sigma_c^2$ also exhibits an increasing trend in error ratio with higher standard deviation values, but the rate of increase is more gradual. From a standard deviation of 4 to 6, the error ratio of $\sigma_c^2$ increases by approximately 14% (from 15.10 to 17.29). The subsequent increase from a standard deviation of 8 to 12 is more substantial, but it is still less pronounced compared to the jump in $\eta$'s error ratio. This indicates that while the error ratio $\sigma_c^2$ does increase with higher standard deviation, it does so at a slower rate than $\eta$.

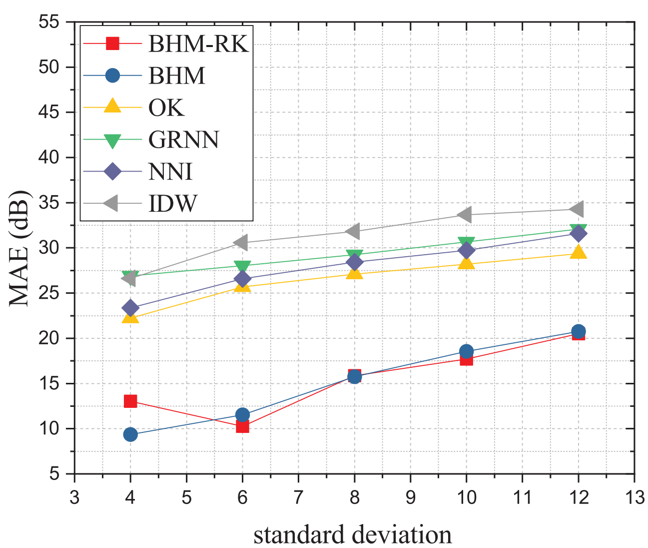


Fig. 7. MAE versus standard deviation with different algorithms, $R = 50$.

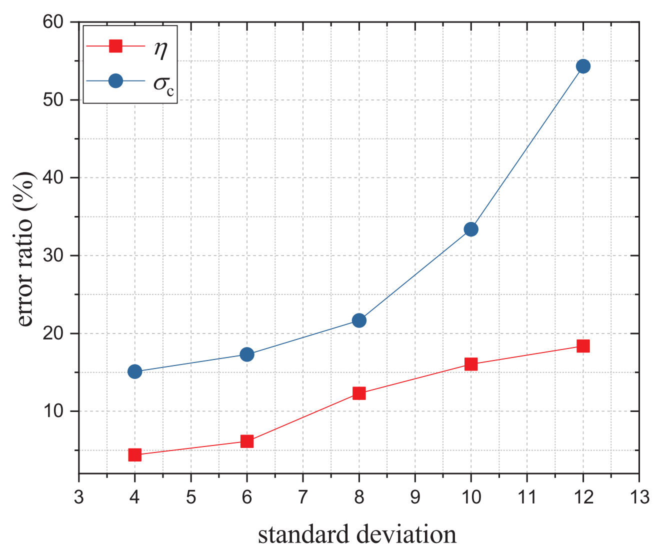


Fig. 8. Parameters error ratio versus standard deviation with different algorithms, $R = 50$.

True values of REM and construction results of all algorithms are displayed in Fig. 9.

### 4.3. *Real-world data test case*

This subsection reports the results of testing REM construction algorithms on real-world data. The measurement sensor was established based on a Keysight Spectrum Analyzer N9935A. To improve the credibility of the real-world data test, we analyzed the measurements gathered within the geographical coordinates ranging from 112°59'20" E to 112°59'26" E longitude and 28°13'14" N to 28°13'20" N latitude in April 2022. The testing frequency was configured at 2.63 GHz, aligning with China Mobile's 5G downlink frequency band, and the power spectrum of a certain sensor is displayed in the left subfigure of Fig. 10.

Based on cost considerations, the sensor was integrated into a vehicle-based system, and measurements were recorded while the vehicle was moving. Because all measurements were completed within a short period of time, the sequential data collected at different locations can be approximately

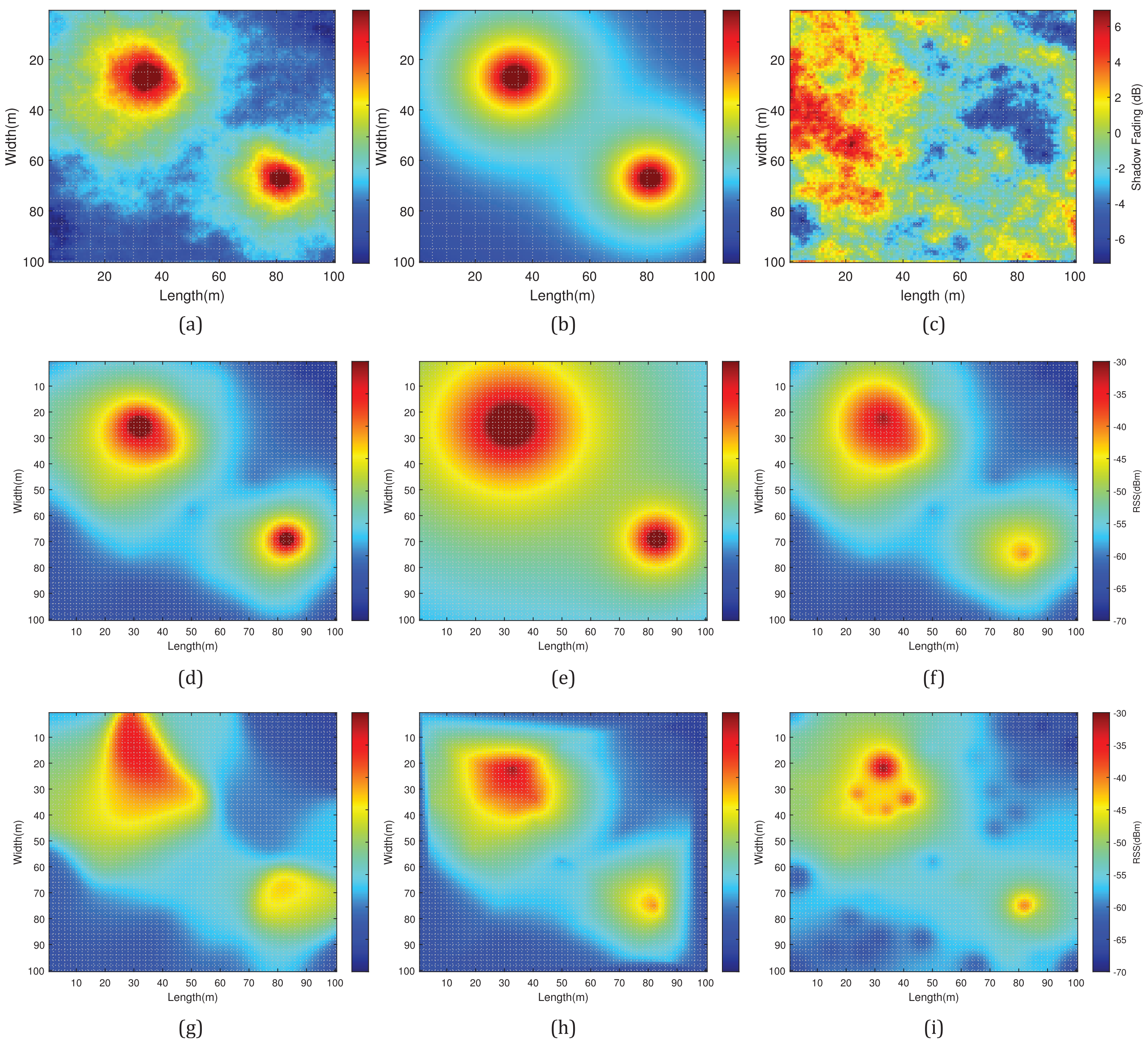


Fig. 9. True values of REM and constructed REMs by different algorithms, $\sigma_c^2 = 8$, R = 50. (a) True values of RSS. (b) Shadow fading components. (c) Pathloss components. (d) BHM-RK. (e) BHM. (f) OK. (g) GRNN. (h) NNI. (i) IDW.


Fig. 10. Schematic illustration: (left) the power spectrum of a certain sensor, (mid) illustration of the locations of some sensors and (right) REM construction results of a specific area.

considered to have been measured simultaneously by numerous sensors, and the illustration of the locations of some sensors is displayed in the middle subfigure of Fig. 10.

In order to enhance the objectivity of the real-world test, the measurements were divided into a validation set and a test set. The validation set aimed for a spatially uniform distribution to depict the comprehensive RSS condition within the experimental area. Throughout the testing phase, the test set was employed for constructing REM for various methods under varying sensor number conditions using the Monte Carlo method. Figures 11 and 12 demonstrate the RMSE and MAE plotted against the sensor number for different algorithms, respectively.

Regarding the overall trend across different number of sensor values, it was observed that as number of sensors increased, BHM-RK consistently outperformed other techniques, showcasing a decreasing trend in both RMSE and MAE. In contrast, some methods such as IDW displayed fluctuating RMSE values, while others like GRNN and NNI showed a more stable but comparably higher RMSE across different number of sensor settings.

In the conducted analysis, the BHM-RK method demonstrated pronounced advantages over various other methods. Specifically, in terms of RMSE, at the number of sensors equaling 50, the BHM-RK methodology exhibited a substantial reduction of approximately 33.0% compared to the BHM. Furthermore, it surpassed the OK by approximately 30.7%, the GRNN by nearly 39.7%, the NNI by about 35.3%, and the IDW technique by roughly 42.3%. Similarly, in assessing MAE, the BHM-RK achieved approximately 11.3% lower error than BHM, 16.0% less than OK, 21.2 lower than GRNN, approximately 19.3 below NNI, and a marked decrease of 22.3 compared to IDW. These findings underscore the superiority of the BHM-RK in terms of both RMSE and MAE metrics.

The exceptional performance of BHM-RK has validated the efficacy of the BHM for pathloss components. However,

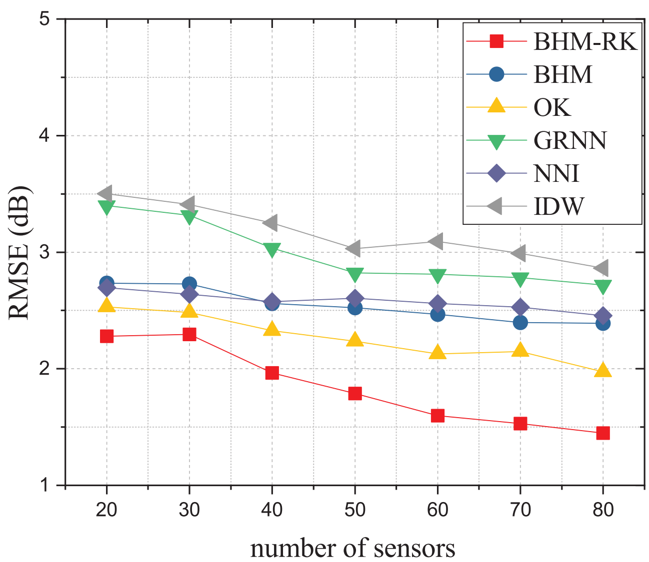


Fig. 11. RMSE versus sensor number with different algorithms.

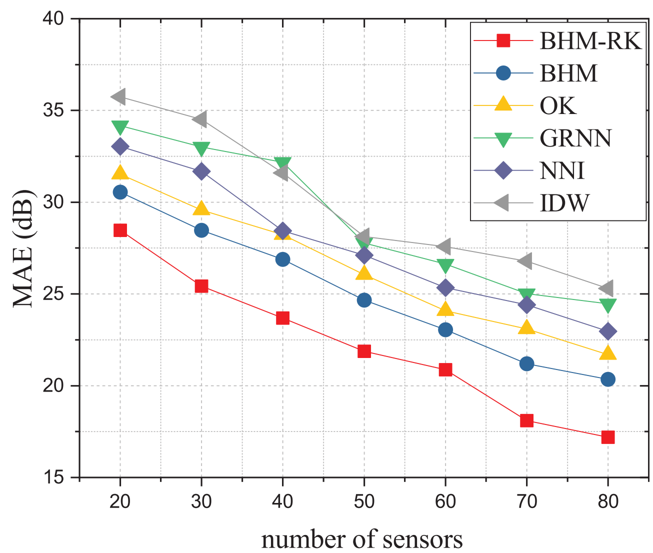


Fig. 12. MAE versus sensor number with different algorithms.

BHM still exhibits inferior performance compared to OK due to the impact of shadow fading components, particularly in urban scenarios we conducted the real-world test. Therefore, BHM-RK's remarkable performance is attributed to the integration of the BHM as well as residual Kriging for different components.

## 5. Conclusion

In this paper, the algorithm proposed, named BHM-RK, introduces a novel approach to constructing REMs tailored for scenarios with multiple transmitters. The algorithm's framework comprises spatial clustering for transmitter partitioning, Bayesian posterior inference within partitions, and residual Kriging interpolation, addressing the challenges posed by diverse transmitter influences.

Through spatial clustering, the algorithm effectively distinguishes transmitter impact ranges, facilitating precise measurement differentiation and establishing a foundation for subsequent BHM construction. The Bayesian posterior inference enables accurate estimation of pathloss components, while the incorporation of residual Kriging based on measurement residuals enhances the estimation of shadow fading components, demonstrating a comprehensive and robust methodology.

Experimental validation involving synthetic and real-world data tests confirms the superior performance of the BHM-RK algorithm in terms of construction accuracy compared to existing methods. This research contributes valuable insights into REM construction methodologies for scenarios with multiple transmitters, underscoring the precision enhancements brought about by the BHM-RK algorithm in radio environment mapping.

## Acknowledgments

This work was supported in part by the National Natural Science Foundation of China (Nos. 61601491 and 62104255) and the Scientific Research Projects of the National University of Defense Technology (No. ZK21-21).

## Appendix A. Posterior Distribution Deduction of Propagation Model Parameters

This appendix describes how to obtain the posterior distribution of $P_t$, $\eta$ and $\sigma_c^2$, respectively. First of all, we defined $DL(r) \doteq \log_{10}(\|l_t - l_r\|/d_0)$.

For $P_t$, by using Bayes rules, the posterior distribution is specified by a simple product of a normal distributive prior and the likelihood, which can be formulated as

$$\begin{aligned}
& f(P_t|\tilde{\mathbf{Z}}, \eta, \sigma_c^2) \\
& \quad \propto f(P_t) f(\tilde{\mathbf{Z}}|P_t, \eta, \sigma_c^2) \\
& \quad \propto \exp\left(-\frac{1}{2\sigma_{P_t}^2} {P_t}^2 + \frac{\mu_{P_t}}{\sigma_{P_t}^2} P_t\right) \\
& \qquad \times \prod_{r=1}^{R} \exp\left\{-\frac{1}{2\sigma_c^2}[z_r - P_t + G_{dB} + 10\eta DL(r)]^2\right\} \\
& \quad \propto \exp\left(-\frac{1}{2\sigma_{P_t}^2} {P_t}^2 + \frac{\mu_{P_t}}{\sigma_{P_t}^2} P_t\right) \exp\left\{-\frac{1}{2\sigma_c^2}\right. \\
& \qquad \left. \times \sum_{r=1}^{R}[{P_t}^2 - 2P_t(z_r + G_{dB} + 10\eta DL(r))]\right\} \\
& \quad \propto \exp\left\{\begin{array}{c} -\dfrac{1}{2}\left(\dfrac{1}{\sigma_{P_t}^2} + \dfrac{R}{\sigma_c^2}\right){P_t}^2 + \\ \left\{\dfrac{\mu_{P_t}}{\sigma_{P_t}^2} + \dfrac{1}{\sigma_c^2}\displaystyle\sum_{r=1}^{R}\left[\begin{array}{c} z_r + G_{dB} \\ +10\eta DL(r)\end{array}\right]\right\} P_t \end{array}\right\}.
\end{aligned} \tag{A.1}$$

Similar to $P_t$, the posterior distribution of $\eta$ can be formulated as

$$\begin{aligned}
& f(\eta|\tilde{\mathbf{Z}}, P, \sigma_c^2) \\
& \quad \propto f(\eta) f(\tilde{\mathbf{Z}}|P_t, \eta, \sigma_c^2) \\
& \quad \propto \exp\left(-\frac{1}{2\sigma_\eta^2}\eta^2 + \frac{\mu_\eta}{\sigma_\eta^2}\eta\right) \\
& \qquad \times \prod_{r=1}^{R} \exp\left\{-\frac{1}{2\sigma_c^2}\left[\begin{array}{c} z_r - P_t + G_{dB} + \\ 10\eta DL(r)\end{array}\right]^2\right\} \\
& \quad \propto \exp\left(-\frac{1}{2\sigma_\eta^2}\eta^2 + \frac{\mu_\eta}{\sigma_\eta^2}\eta\right) \exp\left\{-\frac{1}{2\sigma_c^2}\right. \\
& \qquad \left. \times \sum_{r=1}^{R}\left[\begin{array}{c} (10DL(r))^2\eta^2 + \\ 2\eta(10DL(r)\cdot(z_r - P_t + G_{dB}))\end{array}\right]\right\} \\
& \quad \propto \exp\left\{\begin{array}{c} -\dfrac{1}{2}\left[\dfrac{1}{\sigma_\eta^2} + \dfrac{10}{\sigma_c^2}\displaystyle\sum_{r=1}^{R} DL(r)\right]\eta^2 + \\ \left\{\dfrac{\mu_\eta}{\sigma_\eta^2} - \dfrac{10}{\sigma_c^2}\displaystyle\sum_{r=1}^{R}\left[\begin{array}{c} DL(r)\cdot \\ (z_r - P_t + G_{dB})\end{array}\right]\right\}\eta \end{array}\right\}.
\end{aligned} \tag{A.2}$$

As for $\sigma_c^2$, since the prior is inverse Gamma distribution, $(\frac{1}{\sigma_c^2})$ distributes as Gamma distribution, then the posteriors can be formulated as

$$
\begin{aligned}
&f(\sigma_c^2|\tilde{\mathbf{Z}}, P, \sigma_c^2) \\
&\quad \propto f\left(\frac{1}{\sigma_c^2}\right) f(\tilde{\mathbf{Z}}|P_t, \eta, \sigma_c^2) \\
&\quad \propto \left(\frac{1}{\sigma_c^2}\right)^{\alpha-1} \exp\left[-\frac{1}{\beta}\left(\frac{1}{\sigma_c^2}\right)\right] \\
&\qquad \times \prod_{r=1}^{R} \left(\frac{1}{\sigma_c^2}\right)^{\frac{1}{2}} \exp\left\{-\frac{1}{2\sigma_c^2}\left[\frac{z_r - P_t + G_{dB}+}{10\eta DL(r)}\right]^2\right\} \\
&\quad \propto \left(\frac{1}{\sigma_c^2}\right)^{\alpha-1+\frac{R}{2}} \\
&\qquad \times \exp\left\{-\left[\frac{1}{\beta} + \frac{1}{2}\sum_{r=1}^{R}\left[\frac{z_r - P_t + G_{dB}+}{10\eta DL(r)}\right]^2\right]\left(\frac{1}{\sigma_c^2}\right)\right\}.
\end{aligned} \tag{A.3}
$$

## ORCID

Haiyang Xia https://orcid.org/0000-0002-2739-9002
Song Zha https://orcid.org/0000-0003-4656-1850
Hao Ding https://orcid.org/0000-0003-4585-9743
Jijun Huan https://orcid.org/0009-0000-0272-6444
Peiguo Liu https://orcid.org/0000-0001-5178-6806

## References

[1] M. Pesko, T. Javornik, A. Košir, M. Štular and M. Mohorčič, Radio environment maps: The survey of construction methods, *KSII Trans. Internet Inf. Syst.* **8**(11) (2014) 3789–3809.
[2] T. Tian, X. Huang, Y. Xu, P. Liu, C. Liu, N. Hu, J. Zhang and Z. Wu, A wideband energy selective surface with quasi-elliptic bandpass response and high-power microwave shielding, *IEEE Trans. Electromagn. Compat.* **66**(1) (2024) 224–233.
[3] K. Wen, X. Huang, T. Tian, W. Huang and P. Liu, Design and demonstration of high-power density infrared nonlinear filtering window with EM shielding, *Opt. Express* **32** (2024) 5956–5968.
[4] H. Xia, S. Zha, J. Huang, J. Liu and P. Liu, Spectrum cartography based on dynamic compressed sensing by using multiple domains information, *J. Commun. Netw.* **25**(4) (2023) 507–515.
[5] D. Denkovski, V. Atanasovski, L. Gavrilovska, J. Riihijarvi and P. Mahonen, Reliability of a radio environment map: Case of spatial interpolation techniques, in *Proc. Cognitive Radio Oriented Wireless Networks and Communications (CROWNCOM)*, Stockholm, Sweden, 2012, pp. 248–253.
[6] K. Sato and T. Fujii, Kriging-based interference power constraint: Integrated design of the radio environment map and transmission power, *IEEE Trans. Cogn. Commun. Netw.* **3**(1) (2017) 13–25.
[7] H. Xia, S. Zha, J. Huang and J. Liu, Radio environment map construction by adaptive ordinary Kriging algorithm based on affinity propagation clustering, *Int. J. Distrib. Sens. Netw.* **16**(5) (2020) 1–10.
[8] K. Sato, K. Inage and T. Fujii, On the performance of neural network residual Kriging in radio environment mapping, *IEEE Access* **7** (2019) 94557–94568.
[9] Y. Feng, A. Mignan, D. Sornette and J. Li, Hierarchical Bayesian modeling for improved high-resolution mapping of the completeness magnitude of earthquake catalogs, *Seismol. Res. Lett.* **93**(4) (2022) 2126–2137.
[10] P. Dellaportas and G. O. Roberts, An introduction to MCMC, *Mach. Learn.* **50** (2003) 5–43.
[11] Y. Q. Xu, B. Zhang, G. Ding, B. Zhao, S. Li and D. Guo, Radio environment map construction based on spatial statistics and Bayesian hierarchical model, *IEEE Trans. Cogn. Commun. Netw.* **7**(3) (2021) 767–779.
[12] J. Geweke and H. Tanizaki, Bayesian estimation of state-space models using the Metropolis–Hastings algorithm within Gibbs sampling, *Comput. Stat. Data Anal.* **37**(2) (2001) 151–170.
[13] A. A. Johnson and G. L. Jones, Gibbs sampling for a Bayesian hierarchical general linear model, *Electron. J. Stat.* **4** (2010) 313–333.
[14] H. Xia, S. Zha, J. Huang and P. Liu, Radio environment map construction by residual Kriging based on Bayesian hierarchical model, in *Proc. IEEE Int. Symp. Electromagnetic Compatibility* (IEEE, 2023), pp. 1–6.
[15] D. F. Specht, A general regression neural network, *IEEE Trans. Neural Netw.* **2**(6) (1991) 568–576.
[16] M. Ester, H. Kriegel, J. Sander and X. Xu, A density-based algorithm for discovering clusters in large spatial databases with noise, in *Proc. of the 2nd International Conference on Knowledge Discovery and Data Mining (KDD'96)* (1996), pp. 226–231.
[17] Y. Teganya and D. Romero, Deep completion autoencoders for radio map estimation, *IEEE Trans. Wireless Commun.* **21**(3) (2022) 1710–1724.
[18] M. Gudmundson, Correlation model for shadow fading in mobile radio systems, *Electron. Lett.* **27**(23) (1991) 2145–2146.
[19] G. Zhang, J. Wang, X. Chen, L. Li and S. Li, Spectrum cartography using the variational Bayesian em algorithm, in *Proc. 12th Int. Conf. Wireless Communications and Signal Processing (WCSP)*, Nanjing, China, 2020, pp. 614–619.
[20] E. Isaaks and R. Srivastava, *An Introduction to Applied Geostatistics* (Oxford University Press, New York, 1989).
[21] D. Shepard, A two-dimensional interpolation function for irregularly-spaced data, in *Proc. ACM National Conf.*, New York, United States, 1968, pp. 517–524.

**Xia Haiyang** received the B.E. degree from the College of Electronic Science and Technology, National University of Defense Technology, Changsha, China, 2015. He is currently working toward his master's degree with the College of Electronic Science and Technology, National University of Defense Technology, Changsha, China. His research interests include radio environment map construction, cognitive radio, and radio spectrum sensing and management.

**Zha Song** received the M. S. degree in signal and information processing from the Electronic Engineering Institute (EEI) and Ph. D. degree in electronic science and technology from the National University of Defense Technology (NUDT), in 2010 and 2014, respectively. He is currently a lecturer in NUDT. His research interests include electromagnetic environment sensing and electromagnetic compatibility.

**Hao Ding** received the B.S. and M.S. degree from Air Force Engineering University (AFEU), Xi'an, China in 2013 and 2016, respectively. He received the Ph.D. degree from University and Institute of Microelectronics, Chinese Academy of Sciences (IMECAS), Beijing, China and Air Force Engineering University (AFEU), Xi'an, China in 2020. He is now working as a lecturer in National University of Defense Technology. His research interests include IC and Microsystem designs for electromagnetic compatibility and protection.

**Huang Jijun** received the M.S degree in electromagnetic field and microwave technologies and the Ph.D. degree in electronic science and technology from the National University of Defense Technology (NUDT), in 1997, and 2005, respectively. He is currently an Associate Professor in NUDT. His current research interests include spectrum management and electromagnetic resource optimization.

**Liu Peiguo** received the B.Sc. and M.Sc. degrees in electromagnetic field and microwave technologies and the Ph.D. degree in communication and information systems from the National Universityof Defense Technology (NUDT), Changsha, China, in 1990, 1994, and 2000, respectively. From 2004 to 2005, he was a Visiting Scholar with the University of Calgary, Calgary, AB, Canada. He is currently a Professor with NUDT. His current research interests include electromagnetic radiation, electromagnetic compatibility and protection.